Radioprotection
© SFRP, 2020
https://doi.org/10.1051/radiopro/2020006

Available online at:
www.radioprotection.org

ARTICLE

A new Monte Carlo tool for organ dose estimation in computed tomography

C. Adrien[1], C. Le Loirec[1,*], S. Dreuil[2] and J.-M. Bordy[1]

[1] CEA, List, 91191 Gif-sur-Yvette, France.
[2] Service de physique médicale, Gustave-Roussy, 94805 Villejuif, France.

Received: 18 March 2019 / Accepted: 21 February 2020

Abstract – The constant increase of computed tomography (CT) exams and their major contribution to the collective dose led to international concerns regarding patient dose in CT imaging. Efforts were made to manage radiation dose in CT, mostly with the use of the CT dose index (CTDI). However CTDI does not give access to organ dose information, while Monte Carlo (MC) simulation can provide it if detailed information of the patient anatomy and the source are available. In this work, the X-ray source and the geometry of the GE VCT Lightspeed 64 were modelled, based both on the manufacturer technical note and some experimental data. Simulated dose values were compared with measurements performed in homogeneous conditions with a pencil chamber and then in CIRS ATOM anthropomorphic phantom using both optically stimulated luminescence dosimeters (OSLD) for point doses and XR-QA Gafchromic® films for relative dose maps. Organ doses were ultimately estimated in the ICRP 110 numerical female phantom and compared to data reported in the literature. Comparison of measured and simulated values show that our tool can be used for a patient specific and organ dose oriented radiation protection tool in CT medical imaging.

Keywords: Monte Carlo simulation / computed tomography / organ dose

1 Introduction

Due to the significant rise of computed tomography (CT) exams in the past few years and the resulting increase of the collective dose (Kalender, 2014), patient dose in CT imaging has become a subject of interest in public health, especially for children (Akhlaghi *et al.*, 2015; Journy *et al.*, 2017a, 2017b; Habib *et al.*, 2019). Considerable efforts have thus been made these past few years to manage radiation dose in CT (Coakley *et al.*, 2010; Amis, 2011, Sodickson, 2012; Mayo-Smith *et al.*, 2014). However CT protocols are still traditionally optimized using the CT dose index (CTDI), which is not representative of the patient dose (McCollough *et al.*, 2011; Kalender, 2014). Patient-specific dose reports, including absorbed dose to organs, should thus be suitable for individualized protocol optimization. Because absorbed dose to organ cannot be directly measured, some research groups attempt to adapt the treatment planning system (TPS) used in radiation therapy for kV X-ray beams dosimetry. For example, Alaei *et al.* (2000) investigated the accuracy of a convolution/superposition TPS for predicting kV beam dosimetry, but they reported dose discrepancies up to 145% in the region surrounding bone heterogeneities. Others groups developed specific software based on precomputed Monte Carlo (MC) data, such as CT imaging[1] (Kalender *et al.*, 1999) and ImPact[2]. Axial or helical protocols are included in these software, but large discrepancies can occur for helical acquisitions, since doses are approximated from contiguous axial scan. Instead of approximating dose from precomputed MC data, other research groups developed their own MC software to directly estimate organ dose using computational patient models or patient DICOM images as inputs.

Most of the time, code benchmarking was performed using either a CTDI phantom (Jarry *et al.*, 2003; DeMarco *et al.*, 2005; Deak *et al.*, 2008) or a custom-designed cylindrical phantom which enables dose measurements at seven different radial distances from its central axis (Li *et al.*, 2011). That approach has some limitations because standard and custom-made phantoms are made of PMMA and only permit dose measurements at selected distances from the central axis. Impact of heterogeneities and 2D dose gradients cannot be estimated with such phantoms. Due to the limitations of validation in homogeneous conditions, benchmark in

*Corresponding author: Cindy.LELOIREC@cea.fr

[1] http://ct-imaging.de/en/ct-software-e/impactdose-e.html.
[2] http://www.impactscan.org/.

anthropomorphic conditions is mandatory. For that purpose, DeMarco *et al.* (2005) put MOSFET detectors on the surface of a male anthropomorphic phantom, while Deak *et al.* (2008), as well as Li *et al.* (2011), choose to insert TLD (ThermoLuminescent Dosimeter) chips into Alderson-Rando phantom.

In this work, we present the dosimetric validation of a MC tool based on Penelope (Sempau *et al.*, 2003) by comparing simulated and experimental dose estimations. Without any detailed information provided by the manufacturer, the CT scanner was first modelled only using information provided by the manufacturer technical note and the method proposed by Turner *et al.* (2009). In a first step, the model has been validated in homogeneous conditions by comparing experimental and simulated integrated dose obtained with a pencil chamber. Simulated and measured CTDI values have also been compared. Then point dose measurements in an anthropomorphic phantom, using optically stimulated luminescence detectors (OSLD), were compared with simulated dose values. Dose distributions in the phantom were also measured with Gafchromic XR-QA2 films and compared with the simulated dose distributions to validate the calculated dose gradient in anthropomorphic conditions.

Although anthropomorphic validations are mandatory, they require a detector with weak energy dependence and an accurate calibration for the energy spectra involved in CT. Such conditions are not met nowadays with ionization chamber used in CT. Calibrations are usually performed for one normalized spectrum with uncertainties higher than 3–5% and without any correction factor for other beam qualities. Therefore, given the high number of parameters influencing the measurements and their high uncertainties (about 10% for device parameters such as mAs), 20%-differences between simulated and measured results are generally considered as a good approximation of the real situation and were chosen in the present study as the success criterion.

Finally, as an application case of the tool, we estimated organ doses with a numerical anthropomorphic phantom.

2 Monte Carlo simulation

2.1 CT scanner

The VCT Lightspeed 64 CT scanner (GE Healthcare, Waukesha, WI) is a third-generation scanner. As specified in the technical note, focal spot to isocentre distance is 541 mm. Target is a tungsten-rhenium alloy with a 7 degree tilt angle regarding to reference axis. Dual focal spots are used depending on current and voltage values. According to IEC 60336, small focal spot is 0.7 mm × 0.6 mm and large focal spot is 0.9 mm × 0.9 mm. The beam full width at half maximum (FWHM) is adapted as a function of the focal spot size and the chosen aperture. For a 40 mm beam aperture, the FWHM are 42.6 and 42.9 mm for the small and the large focal spots, respectively. Use of bowtie filter is related to a maximum Scan Field of View (SFOV). The maximum SFOV is 32 cm for the small bowtie filter reported as “Ped Body” and 50 cm for the large bowtie filter reported as “Large Body”. Two tube potentials (100 and 120 kVp), two bowtie filters (“Ped Body” and “Large Body”) and a 40 mm beam collimation are modelled and presented in this work.

Table 1. Filtration of the studied beams.

Potential (kVp)	SFOV (cm)	Total filtration (inherent + central bowtie filtration) (mm Al)
100	50	5.20
120		4.65
100	32	3.44
120		2.89

2.2 CT model

The 2006 release of the MC code Penelope (Sempau *et al.*, 2003) is used to model the VCT Lightspeed 64 CT scanner (GE Healthcare, Waukesha, WI).

For MC simulations, all elements of the X-ray tube need to be modelled. Without any detailed information provided by the manufacturer, filtration elements are modelled by adapting the experimental method described by Turner *et al.* (2009). Based on an initial soft spectrum and experimental data, this method provides information on equivalent inherent filtration and equivalent bowtie filter shapes, which reproduce the attenuation of the real filtration elements. These filtration elements are reported in Table 1. For the bowtie filter only, the central filtration is indicated but the complete equivalent shape is taken into account in the simulation.

One of the specificities of CT scanner is the tube motion of the gantry during the acquisition. Both scanning modes, axial and helical, associated with a specific tube path, have to be carefully implemented into the MC tool. For that purpose, a specific source is defined. Instead of using a direct sampling of particles along the tube path and a limited particle splitting (Li *et al.*, 2011), it was taken advantage of the symmetries in geometry to implement a pipe shaped source with two variance reduction techniques: a circular splitting and a translational one.

The different elements of the X-ray tube are modelled with Penelope according to the manufacturer technical note[3] and to Turner method (Turner *et al.*, 2009) for the filtration. A PSF is created below the bowtie filter at 15 cm from the focal spot (Fig. 1). This PSF contains all the relevant information required to perform the simulation: position, direction, energy, statistical weight, particle type. Each stored particle is read, split and released for simulation.

For the circular splitting, the initial particle is splitted in NC particles. Each splitted particle is sampled on an arc of circle by a random angle (φ) in the interval $[2\pi \times i/N_C : 2\pi \times (i+1)/N_C]$ with i between 0 and $(NC-1)$. User can define NC knowing that a large NC improves the statistics but increases the computation time and might introduce bias in the simulation results. For both scanning modes, X and Y particle coordinates are modified, with X and Y axes the transverse and vertical directions, respectively. In axial mode simulation, the Z coordinate remains unchanged. On the contrary, for helical acquisition, the Z coordinate is modified according to equation (1):

$$z' = z + \varphi/2\pi \times \text{pitch} \times \text{collimation}. \quad (1)$$

[3] LightSpeed ™ VCT – Technical Reference Manual.

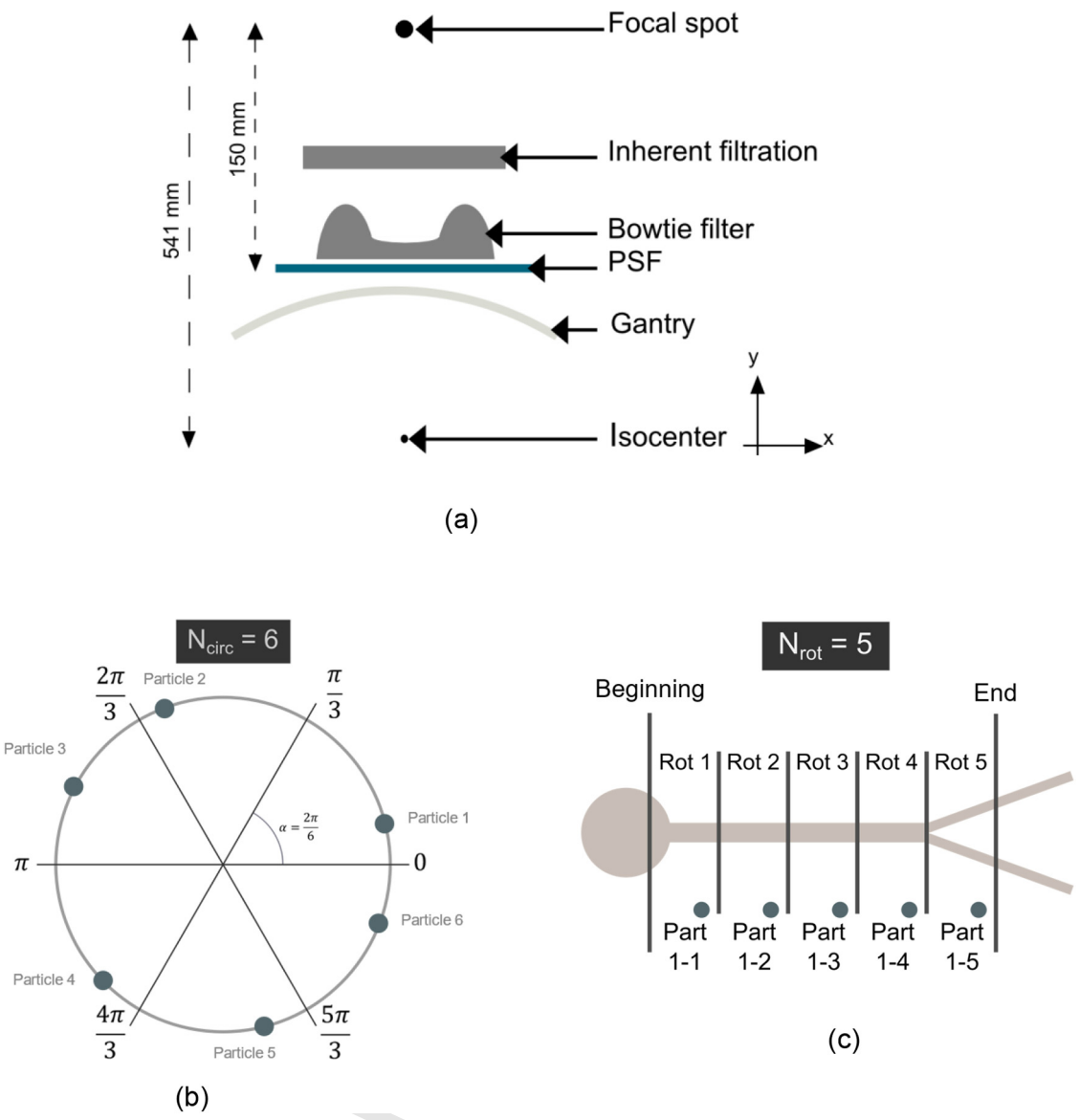

Fig. 1. Information about the CT geometry (a), the PSF location (a), the circular splitting (b) and the longitudinal splitting (c).

Once the circular splitting is realized, each particle is splitted a second time in N_R particles for the translational splitting. The N_R value is determined according to the acquisition parameters as:

$$N_R = \frac{\text{total} \quad \text{explored length}}{\text{pitch} \times \text{collimation}}, \tag{2}$$

so that it allows a complete covering of the scanning range along the Z axis. The new Z coordinate is then determined according to equation (3), placing each NR particle on a gantry rotation.

$$z'' = z' + i \times \text{pitch} \times \text{collimation with } i \in [0, N_R]. \tag{3}$$

Due to the lack of information regarding the tube starting position, which is known to largely influence dose results (Zhang *et al.*, 2009), a unique tube path cannot be determined. Choosing only one tube path can undeniably lead to a dose underestimation/overestimation for some peripheral organs if the real tube motion is largely different of the simulated path. Because a dose underestimation cannot be considered as this tool is designed for radiation protection purposes, choice is made to simulate every possible path. In such a way, dose is systematically overestimated because all peripheral organs will "see" the tube along its path. Tube starting angle is thus randomly chosen for each initial particle.

2.3 Analysis of MC data

The tube loading information is used to normalize MC results. The tube loading can be related to a number of emitted electrons (Ne) according to equation (4), where I represents the CT scanning current expressed in ampere, t the acquisition

Table 2. MC simulation parameters used for the homogeneous acquisitions.

Material	$E_{abs,e-}$ (eV)	$E_{abs,photons}$ (eV)	$E_{abs,e+}$ (eV)	C1	C2	W_{CC} (eV)	W_{CR} (eV)
Air	10^3	10^2	10^4	0.05	0.05	10^2	10^2
PMMA	10^3	10^2	10^4	0.05	0.05	10^2	10^2

time expressed in second, and e the electron elementary charge expressed in coulomb.

$$N_e = \frac{I(\mathrm{A}) \times t(\mathrm{s})}{e}. \quad (4)$$

Emitted primary electrons are actually related to the simulated primary showers in the MC simulation.

2.3.1 Deposited energy in a volume

To validate the MC model in homogeneous conditions a RadCal 10X6-3CT pencil chamber (RTI electronics) is used and modelled as a 10 cm length cylinder. The cylinder radius is the one reported in the chamber documentation. The parameters used for the simulations are reported in Table 2. Elastic-scattering parameters *C1* and *C2* are set to 0.05 to have simulations with the highest precision. Values of the cut-off energies *WCC* and *WCR* are fixed at 100 eV. Absorption energies of 100 keV for electrons and positrons are compatible with the volume of detection as the range of a 100 keV electron is about 0.15 mm in water.

To simulate acquisitions realized with this pencil chamber, integrated dose in the pencil beam is estimated as:

$$DI = \frac{E \times I \times t \times L}{\rho_{\mathrm{air}} \times V \times 10^{-3}}, \quad (5)$$

with DI the integrated dose (in Gy.cm), E the mean deposited energy (in eV/shower) obtained with the MC simulation in the volume represented the pencil chamber, I the scanning current (in A), t the acquisition time (in s), L the chamber length (in cm), ρ_{air} the air density (in g/cm^3) and V the chamber volume (in cm^3).

Uncertainty on the estimated DI is evaluated combining the contributions to the uncertainty budget using the so called "sandwich law" described in the guide to the expression of uncertainty in measurement (ISO/IEC Guide 98-3:2008):

$$\begin{aligned} u_c^2(DI) = & \left(\frac{I \times t \times L}{\rho_{\mathrm{air}} \times V \times 10^{-3}}\right)^2 \times u^2(E) \\ & + \left(\frac{E \times t \times L}{\rho_{\mathrm{air}} \times V \times 10^{-3}}\right)^2 \times u^2(I) \\ & + \left(\frac{E \times I \times L}{\rho_{\mathrm{air}} \times V \times 10^{-3}}\right)^2 \times u^2(t) \\ & + \left(\frac{E \times I \times t}{\rho_{\mathrm{air}} \times V \times 10^{-3}}\right)^2 \times u^2(L) \\ & + \left(\frac{E \times I \times t \times L}{\rho_{\mathrm{air}} \times V^2 \times 10^{-3}}\right)^2 \times u^2(V). \quad (6) \end{aligned}$$

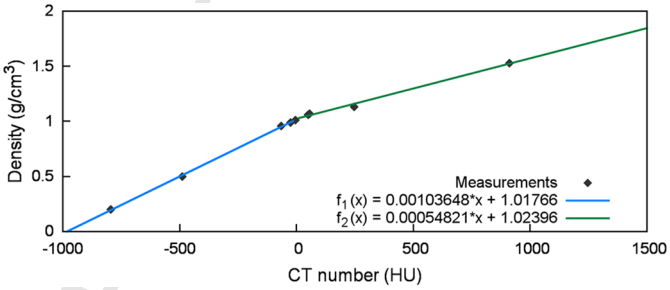

Fig. 2. Calibration function for the DICOM images of the CIRS phantom.

The values of the uncertainties $u(E)$, $u(I)$, $u(t)$, $u(L)$ and $u(V)$ are detailed in paragraph 2.3.3.

2.3.2 Mean dose deposited in a volume

For each CT acquisition with the anthropomorphic phantom, the DICOM images of the CIRS phantom are converted by associating to each Hounsfield Number a MC material. This conversion is done by using a calibration function determined with the CIRS Electron density phantom. The calibration function is reported in Figure 2. Only four materials are considered here: air, bone, soft tissue and lung.

For point doses comparison, the values obtained in the voxels corresponding to inserts containing OSL are compared to measurements.

For dose maps comparison, the values obtained in the pixels of the slices corresponding to the film position are compared to measurements. To do that, dose maps from film read-outs and from MC simulations are centered. As pixel size is not the same between experimental dose map (0.51 mm) and MC simulations (2.9 mm) normalized dose profiles are plotted to compare the results.

To improve the MC computation time for X-ray dosimetric purposes, secondary electrons are not tracked if their range is smaller than the considered voxel size (Deak *et al.*, 2008; Li *et al.*, 2011). The effects of this approximation have already been investigated in detail by Chao *et al.* (2001), who showed negligible differences between incorporating and omitting secondary electrons transport for diagnostic energy beams. The parameters used for the simulation respect this assumption. They are reported in Table 3 for each material.

To validate the MC model in the anthropomorphic phantom, the mean dose in a voxel has to be estimated as:

$$D = D_{MC} \times I \times t \times 1000, \quad (7)$$

with D the dose in the voxel (in G_y), D_{MC} the estimated MC dose value (in eV/g/shower), I the scanning current (in A) and t the acquisition time (in s).

Table 3. Parameters used for PENELOPE simulations and for each biological material used in this study.

Material	$E_{abs,e-}$ (eV)	$E_{abs,photons}$ (eV)	$E_{abs,e+}$ (eV)	C1	C2	W_{CC} (eV)	W_{CR} (eV)
Air	2×10^5	10^2	2×10^5	0.05	0.05	10^2	10^2
Lung	2×10^5	10^2	2×10^5	0.05	0.05	10^2	10^2
Soft tissue	2×10^5	10^2	2×10^5	0.05	0.05	10^2	10^2
Bone	2×10^5	10^2	2×10^5	0.05	0.05	10^2	10^2

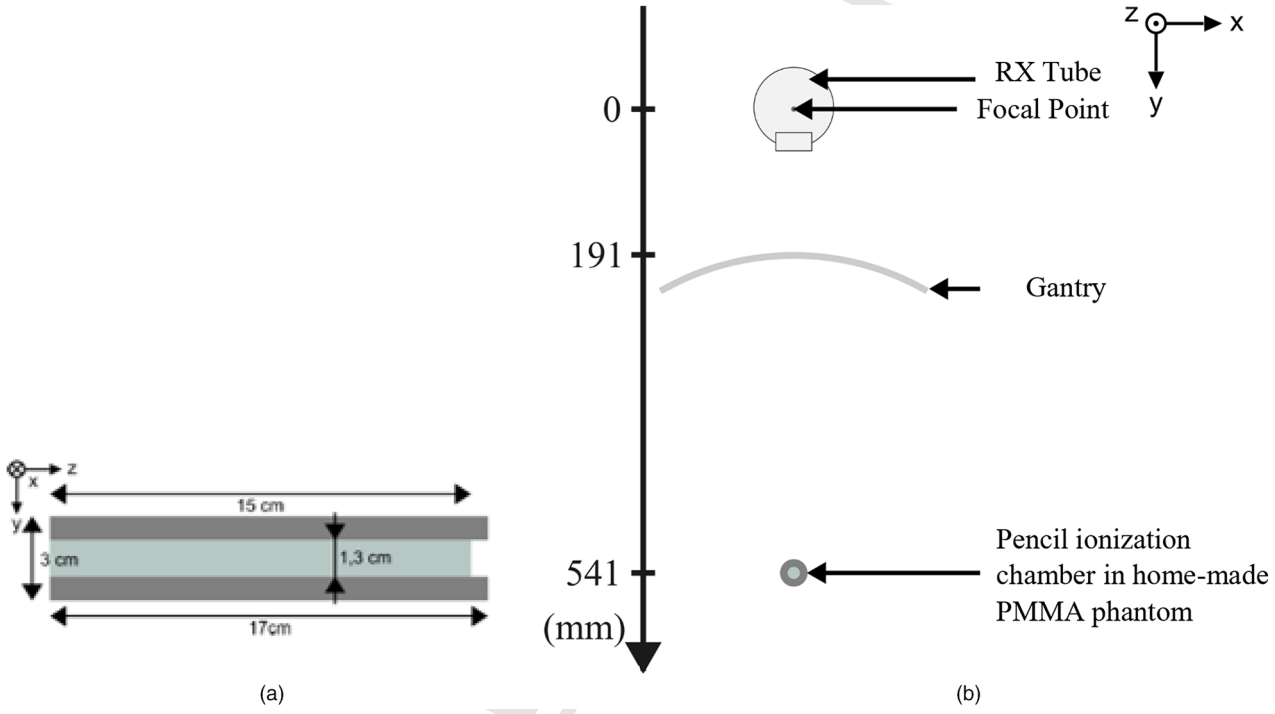

Fig. 3. Longitudinal section of the PMMA phantom (a) and experimental set-up diagram (b).

Uncertainty on the estimated D is also evaluated combining the contributions to the uncertainty budget using the so called "sandwich law" described in the guide to the expression of uncertainty in measurement:

$$u_c^2(D) = u^2(D_{MC}) \times (\mathrm{I} \times \mathrm{t} \times 1000)^2 + u^2(\mathrm{I}) \times (D_{MC} \times \mathrm{t} \times 1000)^2 + u^2(\mathrm{t}) \times (D_{MC} \times \mathrm{I} \times 1000)^2. \quad (8)$$

The values of the uncertainties $u(DMC)$, $u(I)$ and $u(t)$ are detailed in paragraph 2.3.3.

2.3.3 Uncertainty budget

The stochastic uncertainties $u(E)$ and $u(DMC)$ due to MC simulation vary for each simulation. It is given with a coverage factor k = 3. Uncertainty of the current ($u(I)$) and the acquisition time ($u(t)$) are given in the technical note of the CT:

$$u(I) = \mp(10\% + 0.5\mathrm{mA}), \quad (9)$$

$$u(t) = \mp(5\% + 10\mathrm{ms}). \quad (10)$$

However, the confidence interval associated with these uncertainties is not specified. According to the recommendations of the guide for the expression of measurement uncertainty, we decided to consider that the uncertainties were expressed for a confidence interval of k = 1 and that the variable follows a uniform probability law. No information about $u(V)$ and $u(L)$ are given. According to the accuracy needed to build such ionization chamber, we assume that these uncertainties can be considered as negligeable.

Uncertainties are combined with the same confidence interval. In the following they are presented at k = 2, *i.e.* with a confidence interval of ≈ 95%.

It is also considered that all the variables are independent that is to say that the covariance is not taken into account, this can lead to overestimate the uncertainties. It is assume that this overestimate is not large.

3 Model validation in homogeneous conditions

3.1 Isocenter validation

Integral of the air kerma over 100 mm is measured with a 10X6-3CT Radcal pencil ionization chamber (Fig. 3a). The

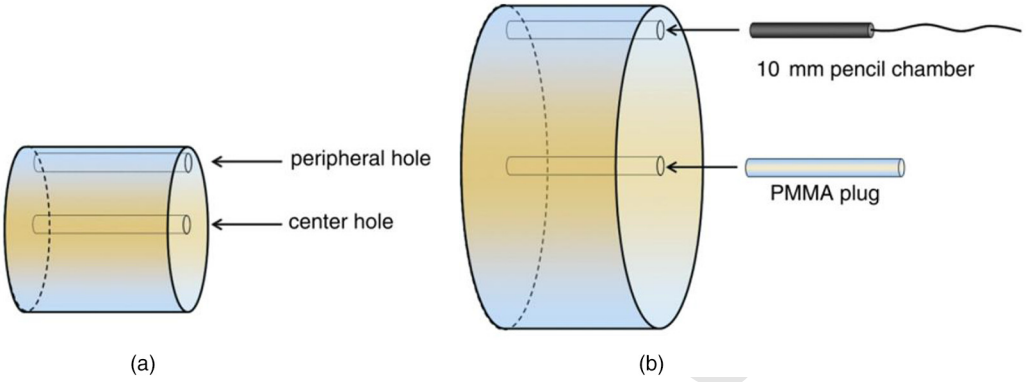

Fig. 4. Layout of the head (a) and body (b) phantoms used for measuring $CTDI_W$.

chamber is introduced into a home-made PMMA tube of 3 cm exterior diameter. Acquisitions have been performed at 100 kVp and 120 kVp, with both bowtie filters, a 40 mm nominal collimation, a 50 cm beam length, 300 mAs and the X-ray tube positioned at the top of the gantry (Fig. 3b).

3.2 "Air kerma" index validation

"Air kerma" index is a dose metric of the CT which represents the amount of radiations emitted per rotation of the RX tube. To determine "air kerma" index, two cylindrical phantoms (Fig. 4) composed of one central inserts and 4 peripheral inserts are used:

- the "head phantom" (Fig. 4a) has a diameter of 16 cm. It is used to calculate the air kerma index for head and children CT acquisitions;
- the "body phantom" (Fig. 4b) has a diameter of 32 cm. It is used to determine the air kerma index for body CT acquisitions.

The air kerma index *CTDIW* (for Weighting Computed Tomographic Dose Index) is defined as:

$$CTDI_W = \frac{1}{3}\left(C_{PMMA,100,c} + 2 \times C_{PMMA,100,p}\right), \qquad (11)$$

with $C_{PMMA,100,c}$ being the value of the air kerma index obtained when the pencil chamber is localized in the central location and $C_{PMMA,100,p}$ being the mean value of the air kerma index when the pencil chamber is inserted in the 4 peripheral locations.

Acquisitions have been performed at 100 kVp and 120 kVp and for a 40 mm nominal collimation. The bowtie filter corresponding to the phantom has been used, thus the Ped Body filter for the head phantom and the Large Body filter for the body phantom. All acquisitions have been performed with the Radcal pencil chamber, 600 mA and an acquisition time of 1 s. The phantom is positioned at the CT isocenter. The pencil chamber is positioned in one of the insert while the other inserts are filled with PMMA cylinders. Five acquisitions are needed to get the air kerma index in the 5 inserts of each phantom.

Table 4. Acquisitions performed experimentally and with the MC simulation to estimate point dose values.

kVp	Bowtie filter	Pitch	mAs
100	Large	0.984	570
		1.375	750
	Ped	0.516	95
120	Ped	0.984	150

3.3 Uncertainty budget

Measurements uncertainties are evaluated from information reported in the AIEA report 457 about the dosimetric practice in diagnostic imaging (IAEA-TRS 457). Scenario 1 has been chosen to estimate the uncertainty budget. In this scenario, the device is used in conformity with the CEI 61674 norm. According to the data reported in the AIEA report and to the fact that the pencil chamber is inserted in a PPMA phantom, experimental results are presented with a relative uncertainty of 13.3%.

4 Model validation in clinical conditions

Several acquisitions (Tab. 4) are performed combining different parameters (high voltage, pitch, SFOV).

4.1 CIRS anthropomorphic phantom

The ATOM adult female phantom from CIRS is used to perform measurements with optically stimulated luminescence dosimeters (OSLDs). This phantom has slots in different localizations and tissues to insert OSLDs (Fig. 5). In Table 5 are reported the positions of the inserts in which OSLDs have been inserted for both acquisitions (head and thorax).

4.2 OSL dose assessment

In their review, Yukihara and McKeever (2008) show the possibility of using OSLD for CT dosimetry. The great advantages of these detectors are their uniformity in sensitivity

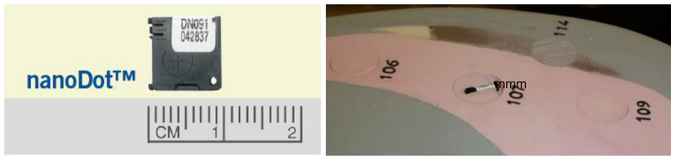

Fig. 5. Photo of an OSLD on the left and photo of an OSLD inserted in a CIRS phantom slot on the right.

Table 5. OSLD locations in the anthropomorphic phantom for thorax and head acquisitions.

	Location	Tissue	Section	Position
Thorax	Stomach	Soft tissue	21	137
	Right Lung	Lung	20	107
	Spine	Bone	19	102
	Heart	Soft tissue	16	83
	Rib	Bone	15	69
Head	Brain	Soft tissue	3	6
	Skull	Bone	3	10
	Mandible	Bone	7	18
	Thyroid	Soft tissue	10	28

because the Al_2O_3:C powder used in the production process is a homogenized mixture of different crystal growth runs. The NanoDot™ (Landauer Inc.) contain single circular OSLD (5.0 mm in diameter) placed in an adapter. An effective depth of 0.1 g/cm^3 is assumed as the point of measurement. Yukihara and McKeever mention the OSLD energy dependence, showing variations between 20 and 30% for potentials ranging from 80 to 140 kVp. We have thus developed a specific user guide to take into account this energy dependence.

4.2.1 Detector calibration

The read-out is performed with the semi-automatic reader MicroStar™ NanoDot™ system. Depending on the dose level, two light intensities are possible: for low doses (< 200 mGy) all 38 LEDs are used and for high doses only 6 LEDs are used. For our application, the reader is always used in the low dose regime.

A calibration of our own OSLD has been carried out on a range from 0 to 150 mGy. Five radiation qualities (^{137}Cs source, ^{60}Co source, RQR 4, RQR 6 and RQR 9 [NF EN 61267 Norm]), available at the French national metrological laboratory (Laboratoire national Henri Becquerel, LNHB), are used. Five detectors have been irradiated for each air kerma value. Average OSLD readings are used to calculate the calibration factor for each beam quality, assuming that OSLD response is linear in terms of air kerma. Results are reported in Table 6.

4.2.2 Detector read-out analysis

Irradiated OSLD, used for measurement, as well as non-irradiated OSLD, are read three times. Mean reading values for irradiated (r_I) and non-irradiated OSLD (r_{NI}) are then computed. These mean raw reading values are then corrected

Table 6. Calibration function (OSLD reading as a function of air kerma) obtained for the different beam qualities.

Beam quality	Calibration function
RQR 4	$R = 6781.4 \times K_a + 2475.5$
RQR 6	$R = 6210.6 \times K_a + 2528.5$
RQR 9	$R = 5551.5 \times K_a + 2647.1$
^{137}Cs	$R = 2007.6 \times K_a + 2573.1$
^{60}Co	$R = 1949.6 \times K_a + 2531.6$

individually from the OSLD sensitivity (*se*) to obtain the real reading value for irradiated (R_I) and non-irradiated (R_{NI}) OSLD, respectively. Finally, the corrected signal *S*, used to determine the dose absorbed by the OSLD is calculated by subtracting raw reading values for irradiated (R_I) and non-irradiated (R_{NI}) OSLD.

To take into account the energy dependence of the OSL detectors, protocol detailed in Bordy *et al.* (2013) is adapted. The energy spectrum corresponding to the OSL position is determined by MC simulation. Calibration factors for each energy bins are convolved using the energy spectrum as weight to adapt the calibration factor to the spectrum at the point of measurement. Assuming the electronic equilibrium condition are fulfilled, the dose in the tissue is obtained by multiplying the air kerma by the ratio of the interaction coefficients:

$$D_{\text{medium } m,Q} = K_{\text{air},Q0} \times \left(\frac{\mu}{\rho}\right)^{Q,m}_{Q0,\text{air}},$$

with $\left(\frac{\mu}{\rho}\right)^{Q,m}_{Q0,\text{air}} = \left(\frac{\mu_{en}}{\rho}\right)_{Q,m} \Big/ \left(\frac{\mu_{tr}}{\rho}\right)_{Q0,\text{air}}$.

4.2.3 Uncertainty budget

For each step of the OSLD read-out, an uncertainty budget is calculated. At the end, the uncertainty associated to the absorbed dose (*D*) in the medium is defined as:

$$U_D^2 = U_K^2 \left[\left(\frac{\mu}{\rho}\right)^{Q,m}_{Q0,\text{air}}\right]^2 + U^2_{(\mu_{en}/\rho)Q,m}\left[\frac{K}{\left(\frac{\mu_{tr}}{\rho}\right)_{Q0,\text{air}}}\right]^2 + U^2_{(\mu_{tr}/\rho)Q0,\text{air}}\left[\frac{K \times \left(\frac{\mu_{en}}{\rho}\right)_{Q,\text{m}}}{\left(\frac{\mu_{tr}}{\rho}\right)^2_{Q0,\text{air}}}\right]^2. \quad (13)$$

with *UK* the uncertainty associated to the air kerma and defined as:

$$U_K = \left(\frac{1}{a_Q}\right)^2 \times U_S^2 + \left(\frac{-S}{a_Q^2}\right)^2 \times U^2_{aQ}, \quad (14)$$

where UaQ is the uncertainty associated to aQ the slope of the calibration function corresponding to the energy spectrum observed at the point of measurement and defined as:

$$U_{\text{aq}}^2 = \left(\frac{1}{\sum_i N_i \times E_i}\right)^2 \sum_i \left(N_i \times E_i \times U_{a(Ei)}\right)^2, \quad (15)$$

and U_S is the uncertainty associated to the OSLD read-out:

$$U_S^2 = U_{\overline{R}_I}^2 + U_{\overline{R}_{NI}}^2, \quad (16)$$

with $U_{\overline{R}_I}$ being the uncertainty associated to the irradiated detectors and $U_{\overline{R}_{NI}}$ being the uncertainty associated to the non-irradiated detectors; both of them are calculated thanks to the following equation:

$$U_{\overline{R}}^2 = \left(\frac{1}{se}\right)^2 \times U + \left(\frac{U_{\overline{r}}}{se \times se}\right)^2 \times U_{se}^2. \quad (17)$$

The uncertainty on the mass interaction coefficients is taken equal to 1%, according to the NIST (https://www.nist.gov/).

4.3 Dose maps assessment with XR-QA films

When exposed to radiation, the organic based dye of radiochromic films changes color due to polymerization: the color of XR-QA films turns from orange to brownish-black depending on the level of exposure (see Fig. 6). Several features of these detectors have attracted the attention of the medical physics community: insensitivity to visible light, self-developing characteristics, dose-rate independence.

Rampado *et al.* (2006) studied the dependence of XR-QA films for kilovolt energies and they proposed a method to use these films (reading, calibration, uncertainties assessment). They also highlighted a variation of the film response with beam energy which can go up to 20%. Boivin *et al.* (2011) proposed also to use the films for *in vivo* dosimetry purposes in medical imaging. More recently, Tomic *et al.* (2014) proposed a method for calibrating and correcting the film reading. They showed that the use of a single calibration function leads to a relative uncertainty of 14% on the dose values, if the calibration function is obtained for a beam quality taken in the middle of the investigated energy range. In the following, we have considered this value for the uncertainty associated to the film analysis.

4.3.1 Film calibration

The films calibration has been carried out in the LM2S (Laboratoire modélisation, systèmes et simulation) laboratory for a 120 kVp X-ray beam with a HVL of 7.14 mm aluminum. Films and a Farmer 30013 PTW ionization chamber have been irradiated at the same time in order to determine the air kerma associated to the film read-out. The Farmer chamber has been previously calibrated at the French national laboratory of metrology (LNHB) in terms of air kerma. Films are read before and one week after irradiation and saved as TIF files. Unirradiated film reading is also necessary to obtain net optical density. It is also recommended to control time between irradiation and read-out (at least 24 h). By using only the red channel, the mean pixel values before (PV_{NI}) and after (PV_I) irradiation are calculated in a mean 1 mm^2 region of interest. The net optical density is then defined in equation (17):

$$\text{net}OD = \log_{10}\left(\frac{PV_{NI}}{PV_I}\right). \quad (18)$$

The calibration function linking the air kerma and the netOD has been adjusted according to the following polynomial function (Eq. (18)):

$$K_{\text{air},Q0} = a \times \text{net}OD + b \times \text{net}OD^4. \quad (19)$$

As for OSLD, the dose in the tissue is obtained by multiplying the air kerma by the ratio of the mass interaction coefficients.

4.3.2 Film analysis

Gafchromic XR-QA2 films are irradiated to study the dose gradient. Films are cut to fit the anatomical shapes of the female anthropomorphic phantom and placed between two phantom slices. For thorax acquisitions, films cannot be inserted into the breasts of the phantom because breast are made from a single piece without any insert or slice. Stencil of the films contours are used to ensure the reproducibility of the film positioning during the reading steps before and after irradiation. For all acquisitions, the tube speed is fixed at 0.7 s/rot and the films are read four times before and one week after the irradiation. Films are read several times to ensure that film storage and handling have been performed in good conditions (dry and dark environment, no dust or fingerprints...). Optical density values are then converted into air kerma according to the calibration function.

A thoracic and a head acquisition (Tab. 7) have been performed.

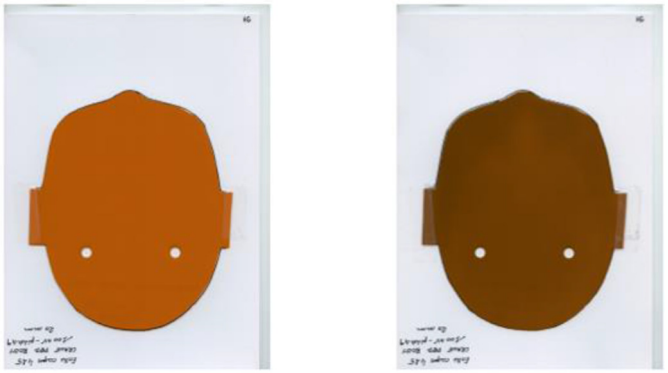

(a) (b)

Fig. 6. Film read-out for the head acquisition: The color of XR-QA films turns from orange to brownish-black. (a) before irradiation; (b) after irradiation.

5 Organ dose estimation

Organ doses for a thoracic localisation have then been estimated into the female phantom provided in ICRP

Table 7. Acquisitions performed experimentally and with the MC simulation to estimate dose maps.

kVp	Bowtie filter	Pitch	Position in the phantom
100	Large	0.516	Between section 16 and 17
120	Ped	1.375	Between section 7 and 8

Publication 110. Simulations are performed for the Large Body bowtie filter with a 50 cm SFOV, 100 and 120 kVp, a 40 mm collimation adapted to the used focal spot (42.6 and 42.9 mm), three mAs (100, 200 and 300), a 0.7 s/rot tube speed and three pitch values (0.531 – 0.969 – 1.375). Dose values to each voxel across all the voxels belonging to each organ are averaged. According to the organ *wT* factors reported in the ICRP 103 we decided to report the dose absorbed by the more sensitive organs thus the left breast glandular tissue, the stomach wall, the left pulmonary tissue, the esophagus and the spinal cord.

6 Comparison of experimental and simulated results

To compare experimental results (r_{exp}, σ_{exp}) and MC estimation (rMC, σMC) we have used 2 index:

– the deviation defined as:

$$\text{dev} = \frac{r_{MC} - r_{exp}}{r_{exp}} \times 100, \tag{21}$$

– and the overlap defined as:

$$ovlp = 100 \times e^{-\frac{(r_{MC}-r_{exp})^2}{2\left(\sigma_{rMC}^2+\sigma_{exp}^2\right)}}. \tag{22}$$

7 Results

7.1 Isocenter experimental validation

Table 8 shows the measured and simulated integral of the air kerma over 100 mm. Results show a good agreement between the simulations and the measurements with a deviation less than 10% and an overlap larger than 87% for the 4 cases considered here.

7.2 Validation of the air kerma index estimation

Table 9 shows the measured and simulated integral of the air kerma index obtained with both phantoms. Results show a good agreement between the simulations and the measurements with a deviation less than 4% and an overlap larger than 89% for the 4 cases considered here.

7.3 Point dose comparison

Experimental and simulated dose values are reported in Figure 7 as well as the relation between them:

$$D_{exp} = 0.867 \times D_{simul}. \tag{23}$$

Simulated values are on average higher than the experimental ones. The uncertainty bars plotted in Figure 7 is obtained by fitting the MC uncertainty associated to each simulated values. This one is about 23.2% (k = 2) for all the simulations performed here. The experimental uncertainty is about 7.4%.

7.4 Dose maps comparison

Experimental and simulated dose distributions for a head scan are reported in Figure 8. Large differences can be observed between the two maps and will be discussed later in the discussion section.

Validation of the dose gradient is performed by comparing simulated and experimental profiles reported in Figure 9 and obtained from Figures 8a–8d. In Figures 8 and 9, the MC uncertainty is about 3% and the experimental uncertainty about 15%. Deviations between simulations and experiments are less than 20% in bone heterogeneities. In soft tissue regions, the deviation can be higher, especially for the head acquisition. This deviation is mainly due to the path of the X-ray tube during the experimental scan which is not simulated accurately in the MC simulation, the initial position of the tube being experimentally unavailable.

7.5 Organ dose estimation

Organ doses for the Large Body Bowtie filter, 120 kVp, 40 mm collimation, 1.375 pitch and 100 mAs, are reported in Table 10 and compared with Zhang *et al.* (2012) results, who also estimated organ dose for the female phantom described in the ICRP 110. They simulated in details the GE VCT LightSpeed 64 thanks to accurate data provided by the manufacturer. They used a modified version of Penelope reported in Li *et al.* (2011) to estimate organ doses in the ICRP 110 phantoms. Our results, obtained in less than one hour in 24CPU for all cases, are a little bit larger than the dose values reported by Zhang *et al.* (2012). Deviations are less than 5.8% for the four organs considered here.

8 Discussion and conclusion

Despite a lack of information about the scanner geometry, the GE VCT LightSpeed 64 has been modelled by adapting the method developed by Turner *et al.* (2009).

Results obtained in homogeneous conditions validate the use of the MC model for dosimetric estimation. Measured and simulated integrals of the air kerma over 100 mm are in agreement; this also validates the use of the tube load information to convert simulated results into Gray. By comparing integral of the air kerma in Table 8 and their associated uncertainties, we note that the simulation uncertainties budget is actually deteriorated by the conversion factor contribution. According to the manufacturer technical note, current and acquisition time have 10% and 5% uncertainty on the displayed value, respectively. Despite these values, relative uncertainties are below 15%. Such uncertainties are compatible with medical imaging applications.

Table 8. Measured and simulated values obtained for the integral of the air kerma in the pencil chamber.

		MC estimation	Experimental value	Comparison	
		DI ± *UDI* (mGy.cm)		Dev. (%)	ovlp (%)
Ped Body Bowie filter	100 kV	289.9 ± 35.1	278.6 ± 18.4	4.0	96.0
	120 kV	400.6 ± 48.4	408.2 ± 26.9	−1.9	99.1
Large Body Bowie filter	100 kV	206.7 ± 25.5	216.1 ± 14.3	−4.4	94.9
	120 kV	309.1 ± 37.8	331.4 ± 21.9	−6.7	87.8

Table 9. Measured and simulated air kerma index obtained with both phantoms.

		MC estimation	Experimental value	Comparison	
		CTDIw ± *UCW* (mGy)		Dev. (%)	ovlp (%)
Ped Body Bowie filter	100 kV	76.3 ± 4.4	74.2 ± 4.9	2.8	95.0
	120 kV	112.9 ± 6.4	117.6 ± 7.8	−4.0	89.4
Large Body Bowie filter	100 kV	37.7 ± 2.6	36.5 ± 2.4	3.2	94.7
	120 kV	58.7 ± 4.0	59.0 ± 3.9	−0.5	99.8

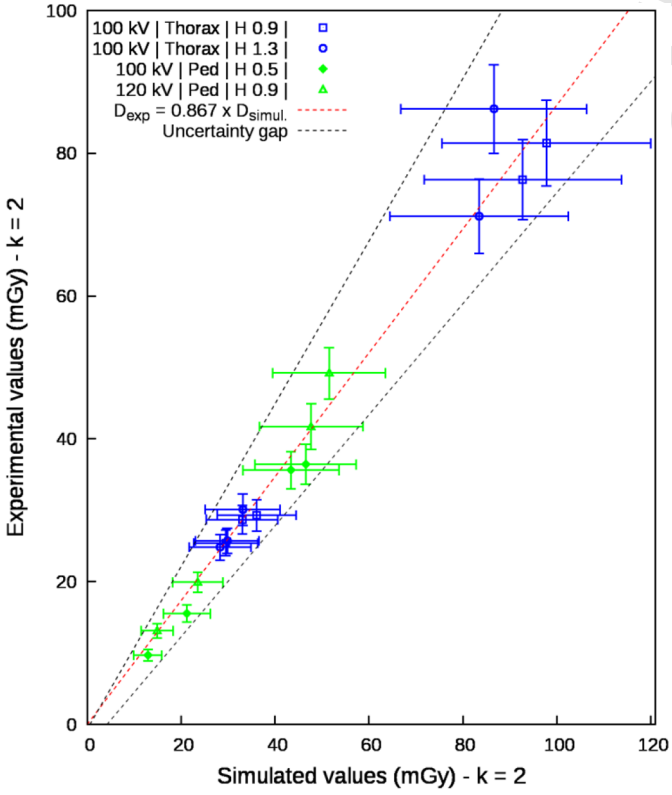

Fig. 7. Experimental dose values *versus* simulated dose values and uncertainties given at k = 2 for the head (in green) and thorax (in blue) acquisitions with the female ATOM phantom. The relation between both dose values is fitted (in red) as well as the uncertainty gap (in black).

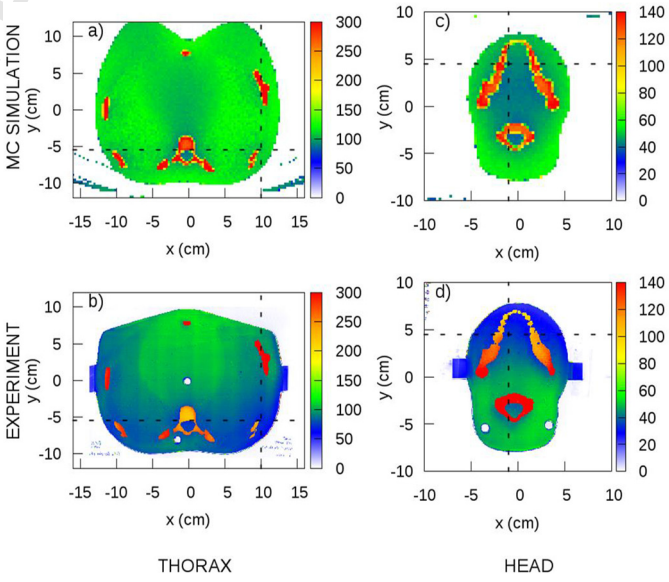

Fig. 8. Simulated and measured dose distributions in mGy for a head (c and d) and a thorax (a and b) scan. Dashed lines indicate the profiles used for Figure 9.

Measured and simulated point dose obtained in anthropomorphic conditions show deviations up to 15%. However confidence intervals are overlapped allowing us to conclude that results are in agreement. The uncertainty budget for simulated doses is mainly by the conversion factor uncertainties. The relative uncertainties for the tube current and the acquisition time

Table 10. Comparison of organ doses for a thoracic helical acquisition obtained with our MC tool and reported by Zhang *et al.* (2012).

	Simulated organ doses (mGy)		
Organs	This study	Zhang *et al.* (2012)	Deviations (%)
Esophagus	9.8 (0.003)	9.3	5.4
Lung	10.9 (0.003)	10.3	5.8
Breast	10.2 (0.002)	10.1	1.0
Stomach	11.1 (0.001)	10.9	1.8

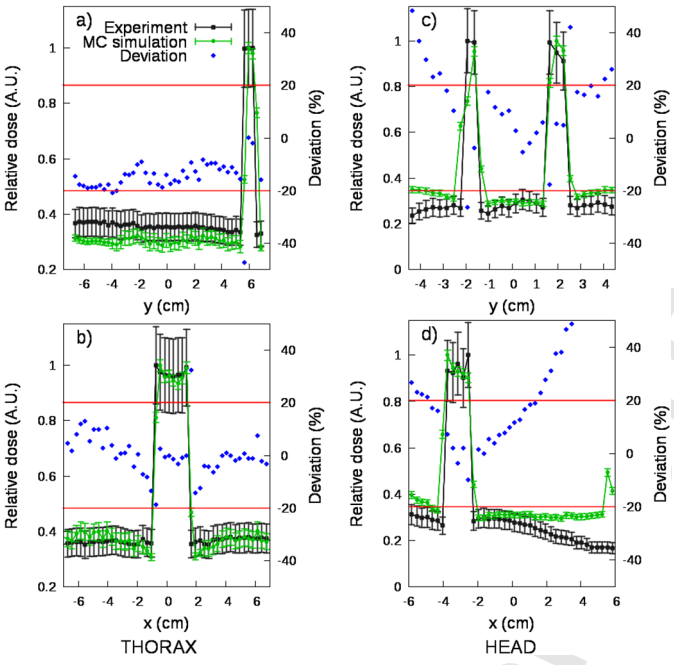

Fig. 9. Simulated and measured relative dose profiles for the head (c and d) and the thorax (a and b) acquisitions. The profiles are obtained for the dashed lines reported in Figure 8. The deviation between simulation and measurement is reported in blue.

are respectively 10% and 5% at k = 1, as reported in the technical note. Simulated dose uncertainties might seem quite large (about 22% at k = 2), but such uncertainties are compatible with dosimetric purposes in medical imaging. The benefit of the conversion factor is therefore maintained.

Large differences in the simulated and the experimental dose distributions can be noted. All the experimental dose maps show an important effect of the initial tube position, as already reported by several authors (Zhang *et al.*, 2009; Li *et al.*, 2011). The surface dose distribution resulting from a helical acquisition is periodic (Dixon and Ballard, 2007) and the tube start angle determines the location of the high and low dose regions. It has been reported by Zhang *et al.* (2009) that the magnitude of organ dose reduction resulting from varying tube start angle varies from 10 to 30% depending on the location and size of the organs. In the experimental dose distribution, shown in Figures 8b and 8d, the tube position relative to the phantom slice containing the film can be easily determined, since a higher dose is delivered to the top and the back of the phantom for the thorax and the head acquisition, respectively. However, the tube path relative to the patient cannot be fully worked out because the tube starting angle information is not provided on the GE VCT Lightspeed 64 scanner. Taking into account this lack of information, it has been decided to randomly sample the tube starting angle for each simulated particle. By making this choice, all possible tube paths are simulated, leading to a more homogenous dose distribution (Figs. 8a and 8c) and an overestimation for some location of the real delivered dose. Nevertheless, instead of underestimating the dose for radiosensitive organs the MC simulation considers the worst case and provides the maximum dose which could be delivered.

For directly irradiated areas there are sometimes some differences in the vicinity of bone structures. They are mainly due to the different pixel sizes between the film and the dose matrices. Due to the small number of particles, the size of the voxels in the dose matrix cannot match the size of that of the film. Indeed, the smaller the size of the voxels, the more one has to increase the number of particles to converge the simulation.

In addition to the difficulties related to the difference in resolution, the dose maps from the simulation highlight problems related to voxelization of the phantom. Since the voxels are larger than those used for the phantom, a voxel in the dose grid can be composed of several tissues (lung, bone and soft tissue in our case). If a voxel is composed of several tissues, it can be considered as being composed of an hybrid tissue associated with an intermediate density according to the densities of the materials initially present and their density. The dose deposit is then affected and the separation between the tissues is less marked. However, the dose profiles show that the gradients are still well respected.

Besides, in their article Long *et al.* (2013) showed from MC simulations that the starting angle could lead to organ dose differences between −20% and 34% compared to the average value. We also found such discrepancies when comparing simulations and measurements obtained with OSLD. By combining the information of Long's article and the non-homogeneous dose deposit visible on the films due to the random draw of the starting position, the important differences found in the comparison between measurement and simulation for the OSLDs can be explained.

For one studied case, organ dose estimations with our software are in agreement with those published by Zhang *et al.* (2012), attesting the reliability of the developed software. Organ dose estimation in the ICRP 110 phantoms can be thus performed in a short notice, less than one hour using 24CPU. In the future, improvements would be considered to reduce the simulation time.

Acknowledgments

The authors thank warmly Helena Chesneau for the calibration of the Gafchromic films and Fabien Moignau, Marc Denoziere, Nelly Lecerf, for their help in the calibration of the OSLD.

Q4 Uncited references

IAEA (2007), ICRP (2007), ICRP (2009), Hubbell and Seltzer (2009) and Sechopoulos et al. (2015).

References

Akhlaghi P, Miri-Hakimabad H, Rafat-Motavalli L. 2015. Dose estimation in reference and non-reference pediatric patients undergoing computed tomography examinations: A Monte Carlo study. *Radioprotection* 50: 43–54.

Alaei P, Gerbi BJ, Geise RA. 2000. Evaluation of a model-based treatment planning system for dose computations in the kilo-voltage energy range. *Med. Phys*. 27: 2821–2826.

Amis ES. 2011. CT Radiation Dose; Trending in the Right Direction. *Radiology* 261: 5–8.

Boivin J, Tomic N, Fadallah B, DeBlois F, Devic S. 2011. Reference dosimetry during diagnostic CT examination using XR-QA radiochromic film model. *Med. Phys*. 38: 5119–5129.

Bordy JM, Bessieres I, d'Agostino E, Domingo C, d'Errico F, di Fulvio A, Knezevic Z, Miljanic S, Olko P, Ostrowsky A, Poumarede B, Sorel S, Stolarczyk L, Vermesse D. 2013. Radiotherapy out-of-field dosimetry: Experimental and computational results for photons in a water tank. *Radiat. Meas*. 57: 29–34.

Chao TC, Bozkurt A, Xu XG. 2001. Conversion coefficients based on the VIP-Man anatomical model and EGS4. *Health Phys*. 81: 163–183.

Coakley FV, Gould R, Yeh BM, Arenson RL. 2010. CT Radiation Dose: What can you do right now in your practice? *AJR* 196: 619–625.

Deak P, van Straten M, Shrimpton PC, Zankl M, Kalender WA. 2008. Validation of a Monte Carlo tool for patient specific dose simulations in multi-slice computed tomography. *Eur. Radiol*. 18: 759–772.

DeMarco JJ, Cagnon CH, Cody DD, Stevens DM, Mc Collough CH, O'Daniel J, McNitt-Gray MF. 2005. A Monte Carlo based method to estimate radiation dose from multidetector CT (MDCT): Cylindrical and anthropomorphic phantoms. *Phys. Med. Biol*. 50: 3989–4004.

Dixon RL, Ballard AC. 2007. Experimental validation of a versatile system of CT dosimetry using a conventional ion chamber: Beyond CTDI [sub 100]. *Med. Phys*. 34: 3399–3413.

IAEA. Technical Reports Series no. 457. 2007. *Dosimetry in diagnostic radiology: An international code of practice*.

ICRP Publication 103. 2007. The 2007 recommendations of the International Commission on Radiological Protection. *Ann. ICRP* 37: 1–332. Pergamon Press.

ICRP Publication 110. 2009. Adult reference computational phantoms. *Ann. ICRP* 39: 1–162. Elsevier.

Habib Geryes B, Hornbeck A, Jarrige V, Pierrat N, Ducou Le Pointe H, Dreuil S. 2019. Patient dose evaluation in computed tomography: A French national study based on clinical indications. *Phys. Med*. 61: 18–27.

Hubbell JH, Seltzer SM. 2009. *Tables of X-ray mass attenuation coefficients and mass energy-absorption coefficients from 1 kev to 20 Mev for elements Z= 1 to 92 and 48 additional substances of dosimetric interest*. Available from http://www.nist.gov/pml/data/xraycoef/index.cfm.

ISO/IEC Guide 98-3. 2008. *Uncertainty of measurement – Part 3: Guide to the expression of uncertainty in measurement (GUM: 1995)*. Joint Committee for Guides in Metrology, JCGM 100.

Jarry G, DeMarco JJ, Beifuss U, Cagnon CH, McNittGray MF. 2003. A Monte Carlo based method to estimate radiation dose from spiral CT: From phantom testing to patient specific models. *Phys. Med. Biol*. 48: 2645–2663.

Journy NMY, Lee C, Harbron RW, McHugh K, Pearce MS, Berrington de Gonzales A. 2017a. Projected cancer risks potentially related to past, current, and future practices in paediatric CT in the United Kingdom 1990–2020. *Br. J. Cancer* 116: 109–116.

Journy NMY, Dreuil S, Boddaert N, Chateil J-F, Defez D, Ducou-le-Pointe H, Garcier J-M, Guersen J, Habib Geryes B, Jahnen A, Lee C, Payen-de-la-Garanderie J, Pracros J-P, Sirinelli D, Thierry-chef I, Bernier M-O. 2017b. Individual radiation exposure from computed tomography: A survey of paediatric practice in French university hospitals, 2010–2013. *Eur. Radiol*. 28: 1432–1084.

Kalender WA. 2014. Dose in X-ray computed tomography. *Phys. Med. Biol*. 59: R129–R150.

Kalender WA, Schmidt B, Zankl M, Schmidt M. 1999. A PC program for estimating organ dose and effective dose values in computed tomography. *Eur. Radiol*. 9: 555–562.

Li X, Segars wP, Surgeaon GM, Colsher JG, Toncheva G, Yoshizumi TT, Frush DP. 2011. Patient-specific radiation dose and cancer risk estimation in CT: Part I. Development and validation of a Monte Carlo program. *Med. Phys*. 38: 397–407.

Long DIJ, Lee C, Tien C, Fisher R, Hoerner MR, Hintenlang D, Boch WE. 2013. Monte Carlo simulations of adult and pediatric computed tomography exams: Validation studies of organ doses with physical phantoms. *Med. Phys*. 40: 013901-1–013901-10.

Mayo-Smith WW, Hara AK, Mahesh M, Sahani DV, Pavlicek W. 2014. How I Do It: Managing Radiation Dose in CT. *Radiology* 273: 657–672.

McCollough CH, Leng S, Yu L, Cody DD, Boone JM, McNitt-Gray MF. 2011. CT Dose Index and Patient Dose: They are not the same thing. *Radiology* 259: 311–316.

Rampado O, Garelli E, Deagostini S, Ropolo R. 2006. Dose and energy dependence of response of gafchromic XR-QA film for kilovoltage X-ray beams. *Phys. Med. Biol*. 51: 2871–2881.

Sechopoulos I, Ali ESM, Badal A, Badano A, Boone JM, Kyprianou I, Mainegra-Hing E, McNitt-Gray MF, McMillan KL, Rogers DWO, Samei E, Turner AC. 2015. *Monte Carlo Reference Data Sets for Imaging Research*. The Report of AAPM Task Group 195.

Sempau J, Fernandez-Varea JM, Acosta E, Salvat F. 2003. Experimental benchmarks of the Monte Carlo code Penelope. *Nucl. Instrum. Methods B* 207: 107–123.

Sodickson S. 2012. Strategies for reducing radiation exposure in multi-detector row CT. *Radiol. Clin. N. Am*. 50: 1–14.

Tomic N, Quintero C, Whiting BR, Aldelaijan S, Bekerat H, Liang L, DeBlois F, Seuntjens J, Devic S. 2014. Characterization of calibration curves and energy dependence GafChromic™ XR-QA2 model based radiochromic film dosimetry system. *Med. Phys*. 41: 062105.

Turner AC, Zhang D, Kim HJ, De Marco JJ, Cagnon CH, Angel E, Cody DD, Stevens DM, Primark AN, McCollough CH, McNitt-Gray MF. 2009. A method to generate equivalent energy spectra and filtration models based on measurement

for multidetector CT Monte Carlo dosimetry simulations. *Med. Phys*. 36: 2154–2164.
Yukihara EG, McKeever SWS. 2008. Optically stimulated luminescence (OSL) dosimetry in medicine. *Phys. Med. Biol*. 53: R351–R379.
Zhang D, Zankl M, DeMarco JJ, Cagnon CH, Angel E, Turner AC, McNitt-Gray MF. 2009. Reducing radiation dose to selected organs by selecting the tube start angle in MDCT helical scans: A Monte Carlo based study. *Med. Phys*. 36: 5654–5664.
Zhang Y, Li X, Segars W, Samei E. 2012. Organ doses, effective doses, and risk indices in adult CT: Comparison of four types of reference phantoms across different examination protocols. *Med. Phys*. 36: 3404–3423.

Cite this article as: Adrien C, Le Loirec C, Dreuil S, Bordy J-M. 2020. A new Monte Carlo tool for organ dose estimation in computed tomography. *Radioprotection*, https://doi.org/10.1051/radiopro/2020006.

Author Queries

Q1 The legends have been removed from the Figures [1, 3, 4, 6] as they are already present in the figure captions. Please check the figures for correctness.

Q2 We have replaced [physcis] by [physics]. Please check for correctness.

Q3 Please check the edits made in figure legend 6 for correctness.

Q4 This section comprises references that occur in the reference list but not in the body of the text. Please position each reference in the text or, alternatively, delete it. Any reference not dealt with will be retained in this section.